World Scientific
www.worldscientific.com

PHASE RETRIEVAL AND INDUCTION MAPPING OF ARTIFICIALLY STRUCTURED MICROMAGNETIC ARRAYS*

V. V. VOLKOV, M. A. SCHOFIELD and Y. ZHU[†]

Brookhaven National Laboratory, Long Island, NY 11973, USA
[†]*zhu@bnl.gov*

We report our study on magnetic structural evolution of artificially patterned micron and submicron magnetic arrays as a function of applied field using *in situ* electron microscopy. To understand magnetic dynamics and switching behavior we employ our newly developed phase retrieval method, based on Lorentz phase microscopy, to map local induction distribution at nanometric scale. We outline the principle of the new method and discuss its advantages and drawbacks in comparison with off-axis electron holography.

Keywords: Lorentz microscopy; *in situ* magnetization; induction mapping; phase retrieval; image processing; off-axis holography.

1. Introduction

Intensive research is underway to understand magnetic-domain configuration and its dynamic behavior, as well as the coupling between magnetic building-blocks of artificially structured assemblies at the nanometric scale. This effort reflects the trend of the ever-decreasing bit-size of the magnetic constituents in recording- and storage-media.[1] It also stimulates continued development of magnetic imaging methods at different length-scales, such as the magneto-optic Faraday and Kerr effects,[2] X-ray magnetic circular dichroism,[3] scanning electron microscopy with polarization analysis,[4] differential phase contrast microscopy,[5] magnetic-force microscopy,[6] and off-axis electron holography.[7] Among them, electron holography offers the opportunity to map local magnetization with a spatial resolution down to a few nanometers and sensitivity of the order of $\pi/100$. The main advantage of electron holography is its quantitative capability for phase-shift retrieval, which provides information on the electrostatic and magnetostatic potential throughout the sample as well as on the fringing field in the regions above and below the sample. While off-axis electron holography has played a crucial role in the nanoscale characterization of domain

---

[†]Corresponding author.

configuration, its application is often hampered by a limited area of view ($< 1 \mu$m in width), especially in characterizing electrostatic potentials of *p–n* junctions in semiconductor devices and the magnetic interactions of micron-size elements. Facing the challenge, recently we developed a phase-retrieval method based on defocused Lorentz Fresnel images. We utilize the Transport-of-Intensity Equation,[8] combined with image alignment, distortion correction and symmetrization algorithms to recover the phase of the object wave and to map local magnetization of the samples.[9] In this article, we first report our observations on the dynamic behavior of magnetic structure of patterned Co elements during a re-magnetization cycle, demonstrating the rich physics involved in the process and the limitations of conventional Lorentz microscopy. We then briefly discuss the theory and applications of our Lorentz-phase microscopy method in revealing the local distribution of magnetization and induction. Finally, we compare the non-interferometric method to off-axis electron holography in studying nanometric permalloy elements.

2. Experimental Details

Films of periodic Co magnetic elements, 1–6 μm in size and 25–40 nm thick, were grown on a 30 nm thick Si_3N_4 membrane supported on a silicon wafer by electron beam evaporation through various shadow masks. Small elements (100–500 nm) of $Ni_{88}Fe_{12}$ permalloy square arrays on a 50 nm thick silicon-nitride membrane were prepared by electron-beam patterning of PMMA photoresist, followed by lifting off the sputter-deposited film. Both kinds of films were deposited in a field-free environment. To prevent charging during exposure to the electron beam, the permalloy samples were coated with a 2 nm thick amorphous carbon layer. The composition of the films was measured by electron-energy loss spectroscopy. *In situ* Lorentz microscopy and phase-retrieval experiments were carried out using a magnetic-field-calibrated JEOL 3000F field-emission transmission electron microscope (TEM),[10] equipped with an electrostatic bi-prism and a Gatan imaging filter. The retractable bi-prism assembly used for electron holography consisted of a platinum wire $< 0.6 \mu$m in diameter, rotatable by $\pm90°$, located approximately in the selected areal aperture plane of the microscope. The images were recorded either on a video tape or a slow scan CCD camera.

3. Observing Magnetization Dynamics Using *In Situ* Lorentz Microscopy

The *in situ* magnetization experiments were performed on samples of a 3 mm disk, consisting of a periodic 2-D array of more than 10,000 Co-elements with a size and spacing of about 6 μm. To apply in-plane magnetic fields using the fields excited by the objective lens of our microscope, we tilted the sample $-30° < \theta < 30°$ at a fixed normal field of $H_0 = 160$ Oe. The set of Lorentz Fresnel images shown in Fig. 1 corresponds to a complete cycle of an *in situ* re-magnetization process under the applied field of $H = H_0 \sin\theta$. To clearly illustrate the dynamic behavior of
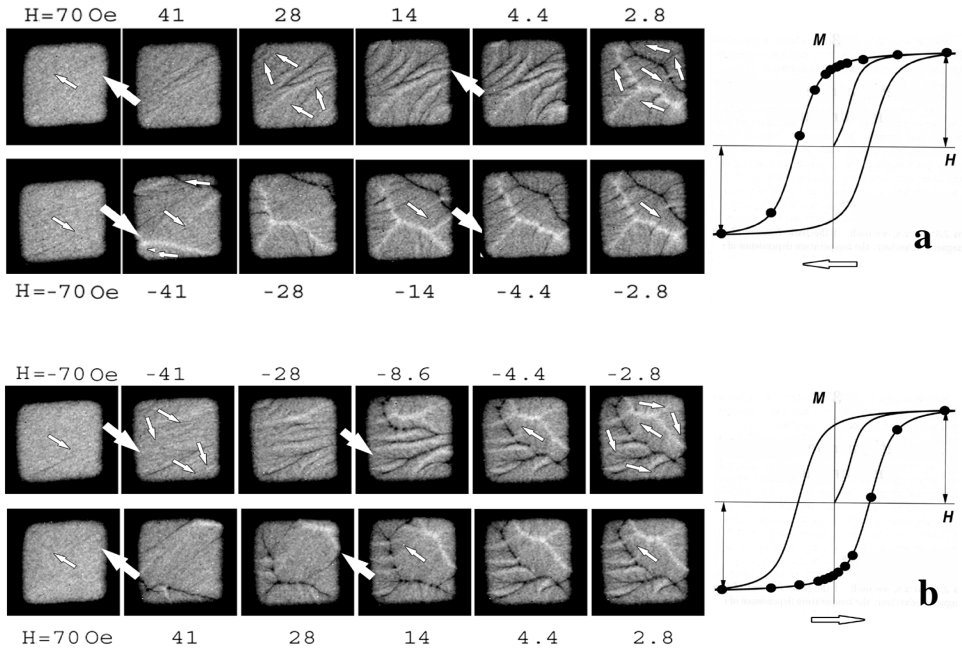
Fig. 1. The evolution of magnetic structure in a 25 nm thick Co-element during magnetization and demagnetization. The sign and amplitude of the applied magnetic field are indicated above or below each image. The large and small arrows show the direction of applied field and local magnetization, respectively. The complete cycle of the corresponding hysteresis loop is shown on the right. The image distortion of the square element at high fields is due to the projection of the sample at a large tilt.

the evolution of the magnetic structure, only one element is shown, with inverted contrast for better visibility. The twelve images of the same element on the top row (Fig. 1(a)) were recorded with applied fields starting at $H = 70$ Oe, and ending at $H = -70$ Oe. The corresponding values of the applied field are indicated above or below each image and their position on the magnetization (M)–field (H) curve is marked by the black dot in the upper part of the hysteresis loop. The reverse process is shown in the bottom set of twelve images (Fig. 1(b)) from $H = -70$ Oe to $H = 70$ Oe, also with the corresponding hysteresis loop on the right. In general, the whole cycle of the re-magnetization process of the 6 μm Co elements can be divided into four steps, according to the sign and amplitude of the applied fields:

(a) $H = 70 \rightarrow 14$ Oe, a process of coarsening and deformation of the magnetic ripple structure (the local magnetization directions, marked by small arrows in Fig. 1, are derived using the phase-retrieval method and will be discussed further in Sec. 5);

(b) $H = 14 \rightarrow 0$ Oe, a process dominated by the nucleation and rapid expansion of the reverse domains with motion of the domain walls and spin-rotation in the remaining domains;
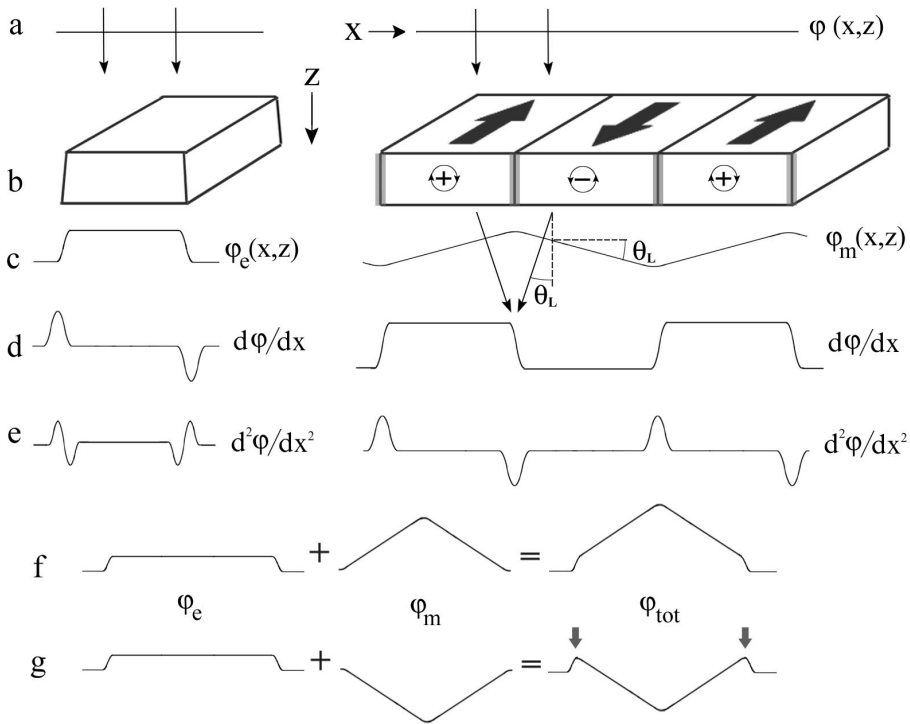
Fig. 2. Schematics of electron-beam deflection and the wavefront curvature due to scattering by pure electrostatic (left) and magnetic samples (right). (a) Original wave front, (b) sample, (c) wavefront at the exit surface of the sample, (d) first derivate of the phase, (e) second derivate of the phase, (f) total phase-profile separated by electrostatic and magnetic component, and (g) total phase profile as (f) but the magnetic component with an opposite magnetization. The phase profile at the sample edge, as marked by the arrow, provides useful information on local magnetization.

(c) $H = 0 \rightarrow -28$ Oe, a process of expulsion of non-favorite domains towards the edges of the Co-element; and,

(d) $H = -41 \rightarrow -70$ Oe, a process of domain-wall annihilation at element edges and completion of the single domain structure. Here, we use Fig. 1(a) as an example; the reverse process (Fig. 1(b)) is very similar.

The occurrence of these steps for individual Co elements is not necessarily identical. The switching fields for domain nucleation and annihilation for each element can differ due to the pre-history and the structural defects of the element as well as its magnetic interaction with neighboring elements. Since these Co-elements are polycrystalline with random crystallographic orientation, wavy-line contrast (Lorentz Fresnel contrast) is the dominant feature in the Lorentz imaging of the sample. This is largely because of the weak magneto-crystalline anisotropy effects determined by the crystal's symmetry (a mixture of cubic and hexagonal), and the high demagnetizing effects determined by the element's shape, or aspect ratio. Unlike

the 180° domain walls observed in highly anisotropic crystals, such as $Nd_2Fe_{14}B$, whose anti-parallel magnetization often is easily defined, details of the magnetic structure associated with faint ripple-contrast is usually difficult to determine. We will show in Sec. 5 that quantitative analysis of ripple contrast is possible with additional defocused Lorentz images using Lorentz-*phase* microscopy that significantly enhances our ability to understand the re-magnetization process.

4. Lorentz-Phase Microscopy

Although Lorentz microscopy is powerful in revealing the movement of magnetic ripples and domain walls in real time, as demonstrated in Fig. 1, it only provides qualitative information in the form of Fresnel contrast at locations where there is a drastic change in magnetization. Information about the amplitude and direction of local magnetization is not available in conventional Lorentz images. As we know, the magnetic vector potential of an object is embedded in the phase of the electron wave passing through the object. The Fresnel contrast in Lorentz microscopy is essentially the second derivative $d^2\phi/dx^2$, or Laplacian, of the phase of the electron wave (Fig. 2). In conventional X-ray- and electron-imaging and diffraction, where the recorded in-focus intensity of an object equals the complex conjugate of its wave function ($I = \psi \cdot \psi^* = Ae^{i\phi} \cdot Ae^{-i\phi} = A^2$), this phase information is lost.

Electron phase retrieval normally requires wave interference using interferometric techniques, as Gabor originally suggested.[11] The ability to accurately measure the spatial distribution of the phase of an object wave function enables us to determine the spatial distribution of electrostatic and magnetostatic potentials in materials that are directly related to their physical properties and functionalities. Several years ago, Paganin and Nugent proposed a non-interferometric phase retrieval formalism[12] based on the so-called Transport-of-Intensity Equation (TIE)[8] that is well known to researchers in light optics. It opened the door to much simpler and less constrained ways to retrieve phase information from an object using traditional microscopy techniques. The TIE relates the change in intensity of an electron wave along its direction of propagation to the change in the phase of the wave in a plane normal to the propagation direction. The equation can be expressed as

$$\nabla_\perp \cdot (I(r,z)\nabla_\perp \phi(r,z)) = -\frac{2\pi}{\lambda}\frac{\partial I(r,z)}{\partial z}, \qquad (1)$$

where ϕ is the phase of the object wave, λ the wavelength of the incident electrons, I the intensity, $\nabla_\perp$ is the 2D gradient operator. The subscript $\perp$ refers to the in-plane coordinates, r, normal to the beam's direction, z. The derivative $\partial I/\partial z$ can be replaced with $\partial I/\partial f$ (f is the focus value in the image plane), well approximated by the difference between two Lorentz, or out-of-focus, images, while the intensity $I(r,0)$ is an in-focus image. Equation (1) suggests that, as a good approximation, the phase of the wave function can be directly retrieved from three images at a small incremental defocus, say $\Delta f = -f, 0, +f$, by applying the inverse Laplacian gradient to the difference of the two out-of-focus images being normalized by the

in-focus image. Demonstrably, the solution of Eq. (1) is unique under Neumann boundary conditions,[9] apart from a constant phase factor.

The electric and magnetic contribution to the electron phase shifts is expressed by the Aharonov–Bohm equation:[13,14]

$$\phi(r) = \phi_E + \phi_M = C_E \oint V(r,z)dz - \frac{e}{\hbar} \iint \mathbf{B}(r,z) \cdot d\mathbf{A} \qquad (2)$$

where $d\mathbf{A}$ is the area element bounded by the beam's path. $C_E = 6.25 \times 10^{-3}$ rad/Vnm for 300 kV electrons, and V and B are the electrostatic potential and magnetic induction, respectively. Figure 2 is a schematic diagram of the phase shift of the electron-beam due to scattering by a pure electrostatic (left) or a pure magnetic (right) sample. As seen, phase is sensitive to a change in both electrostatic and magnetic potentials. There is a phase jump at the sample edges due to the electrostatic potential, while the slope of the phase changes its sign across the domain wall; thus, away from the sample edge, the derivative of the phase $d\phi/dx$ represents the local magnetization, provided the sample has constant thickness. Combining Eqs. (1) and (2), in the area far behind the sample we have[15]

$$\nabla_\perp \cdot (I\nabla\phi_E) + \frac{e}{\hbar}[I\nabla \times t\mathbf{B} + \nabla I \times t\mathbf{B}]_z = -\frac{2\pi}{\lambda}\frac{\partial I(r,z)}{\partial z}\,, \qquad (3)$$

where t is the effective sample thickness and the first and second terms on the left represent the electrostatic and magnetic contribution, respectively. The quantity $t \cdot \mathbf{B}$ is defined as path integral $t \cdot \mathbf{B}(r) \equiv \int \mathbf{B}(r,z')dz'$ along the beam trajectory.

To unravel local magnetization, the electrostatic potential must be separated from the magnetic potentials, especially when small-sized elements are involved. If the thickness t of the element does not vary, the electrostatic contribution will be constant. Alternatively, if V is known, ϕ_E can be accurately calculated for any sample geometry. The advantage of phase retrieval for magnetic applications is that the image wave is, to a very good approximation, equal to the object wave, or exit wave from the sample. Because the scattering angles of the incident electrons from the sample in magnetic imaging is about two to three orders-of-magnitude smaller than the Bragg angles, the spherical aberration of the lenses and the transfer function of the microscope can be neglected. Furthermore, for magnetic elements larger than 6 μm, the electrostatic component is often negligible (less than 2%) compared to its magnetic counterpart. Thus, we can ignore the ϕ_E term, in these cases, to achieve the so-called magnetic transport-of-intensity equation (MTIE):

$$\nabla_\perp \cdot (I\nabla_\perp\phi_M) = -\frac{2\pi}{\lambda}\frac{\partial I(r,z)}{\partial z}\,, \qquad (4)$$

where $\nabla_\perp\phi_M = -\frac{e}{\hbar}[n_z \times t\mathbf{B}]$ with n_z being the unit-vector along the incident beam's direction. Equation (4), although with a form similar to Eq. (1), offers a clear correlation between the phase- and intensity-gradient of the object waves for magnetic materials.
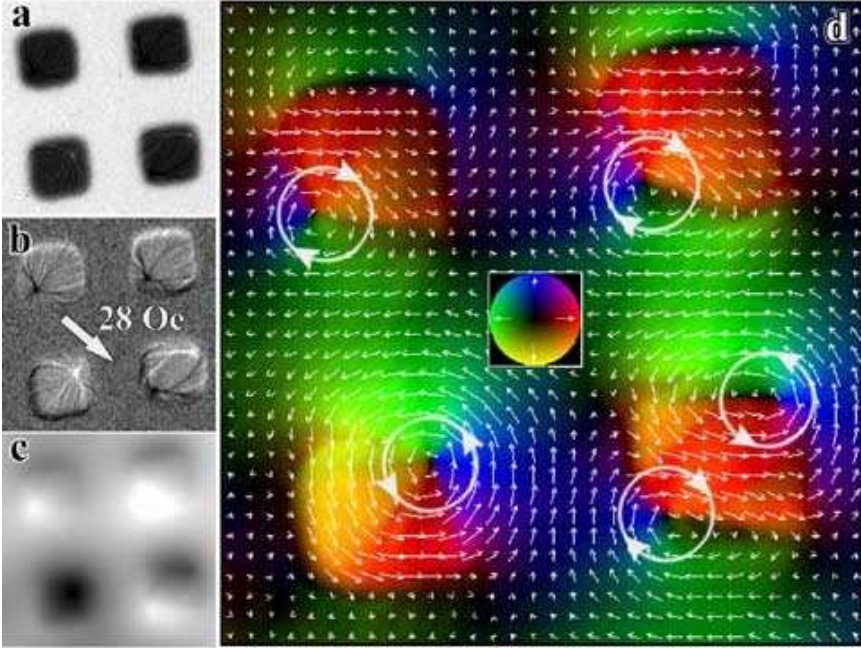
Fig. 3. Fresnel imaging of four Co-elements of 6 μm in size and spacing, patterned on a transparent Si_3N_4 membrane and recorded at $H = 28$ Oe: (a) Experimental defocused image, (b) z-difference image, and (c) reconstructed phase. The image in (d) shows the induction map of recovered electron-wave phase shifts using the MTIE-approach. Color represents the amplitude and direction of the induction vector using the color vector wheel (inset) as the reference.

5. Mapping of Induction Distribution

Figure 3 is an example of our analysis of the artificially structured magnetic array (four 32 nm thick 6 μm × 6 μm Co-elements) using MTIE. Figure 3(a) is an out-of-focus image excerpted from an *in situ* magnetization experiment, recorded with an external in-plane field $H = 28$ Oe. From two such defocused images we can get a difference image, or a z-gradient image (Fig. 3(b)). Using Eq. (4), we are able to retrieve the phase image (Fig. 3(c)) to reconstruct a projected magnetic-induction vector map (Fig. 3(d)), displayed both by arrows and the color-vector notation encoded in the inset. The arrows show the direction and amplitude of local in-plane induction distribution, while the circles highlight a magnetization curling around local vortices in individual Co-islands.

Figure 4 shows the analysis of one snapshot of the dynamic process in Fig. 1 using the MTIE algorithms. Here, two Fresnel images, one is shown as Fig. 4(a), of the Co-elements were used to construct a phase-contrast $\partial I/\partial z$ image (Fig. 4(b)) that is required to solve Eq. (4). Then, the MTIE-reconstructed phase (Fig. 4(c)) was converted into a projected magnetic-induction map, $t \cdot \mathbf{B}(r)$ (Fig. 4(d)). After subtracting the external field, this yields a magnetization map (Fig. 4(e)), including all
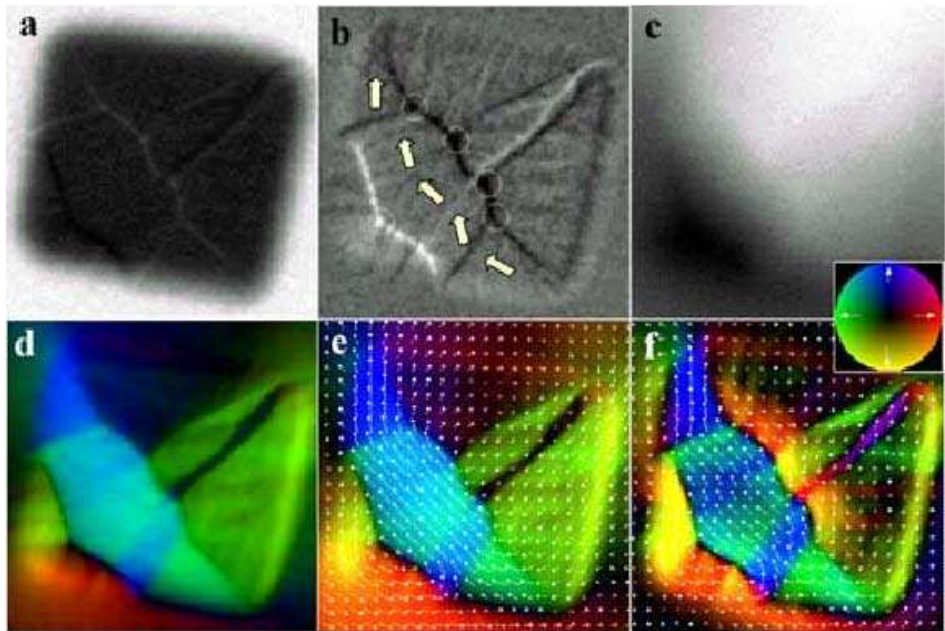
Fig. 4. Analysis of ripple Fresnel contrast in Co-islands, excerpted from the *in situ* experiments shown in Fig. 1. (a) Experimental defocused image, (b) z-gradient image and simple "zig-zag" model of ripple magnetization (shown by arrows), (c) reconstructed phase map, (d) projected in-plane induction, (e) projected magnetization, and (f) high-frequency component of the magnetization map, illustrating by color-vector code the local magnetization of slice nanodomains as the origin of the ripple contrast observed in the experimental images.

demagnetizing fields contributing to the electron-wave's phase shift. This detailed knowledge of local magnetization allows us to interpret the "zig-zag" Fresnel ripple contrast as coherent spin rotation within multi-slice domains away from the applied field's direction, consistent with Hoffmann's prediction.[16] This rotation in each slice domain occurs because of spin-exchange coupling; meanwhile, the effective spin rotation away between the different slice domains in certain fields creates a favorite situation for the nucleation of reverse domains in the central part of Co-islands. Since the Fourier spectrum of any image with fine ripple contrast should have a significant high-frequency component, we filtered out the very low frequencies that are responsible for the long-range demagnetizing fields of the map (Fig. 4(e)) by reducing the intensity of a few pixels close to the origin of the appropriate Fourier power spectrum (only 4×4 pixels out of a total 512×512 size). The remaining spectrum yields the modified magnetization map shown in Fig. 4(f). It is almost free from long-range screening demagnetizing fields and, therefore, presents a color picture of coherent spin alignment within each of the 140–160 nm slice domains, with a very small averaged spin rotation between the slice Co-nanodomains (Fig. 4(b) and (f)). This magnetization ripple is of the same order (~ 160 nm) as reported by Zhou *et al.*[17] It also justifies our initial interpretation of ripple Fresnel contrast (Fig. 1) in
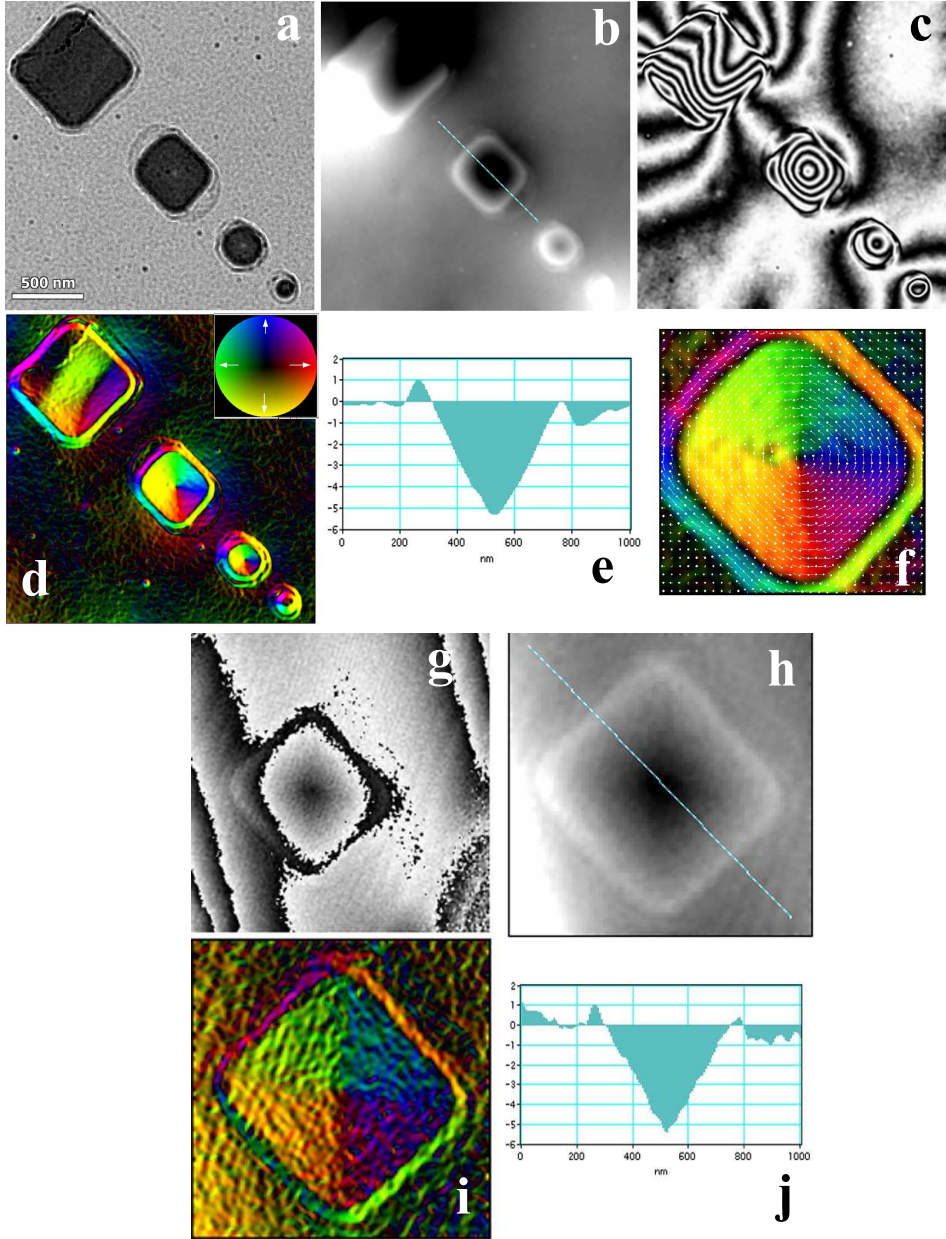
Fig. 5.   A lithographically patterned $Ni_{82}Fe_{18}$ permalloy array. (a) In-focus Lorentz image of the array, (b)–(f) analysis based on the MTIE method, (b) phase image, (c) phase contour map, (d) induction map, color represents the amplitude and direction of the induction using the color vector wheel (inset) as a reference, (e) phase profile of the line scan across the element B in (b), and (f) vector map of the element B, superimposed on the color map. (g)–(j) analysis of element B based on off-axis electron holography, (g) wrapped (h) unwrapped phase image, (i) color induction map, and (j) phase profile of the line scan across the element B in (h).

terms of magnetization ripple, and highlights its important role in reverse-domain nucleation governing the major part of the re-magnetization process in thin film of Co-microelements.

6. Comparison with Off-Axis Electron Holography

To test our MTIE results, we conducted numerous comparisons on the same samples using MTIE analysis and off-axis electron holography. Although the results from both methods agree well, each technique has its own pros and cons, as we stated earlier. In general, MTIE is more versatile in length scale. It's implementation is fast, and does not require special hardware. The speed of the process promises real-time phase-retrieval that is extremely important for studying magnetic dynamics. On the other hand, holography is quantitatively more robust. Quantitative analysis for MTIE can be very demanding; its quality strongly depends on the contrast difference at the periphery of the image,[9] as well as the corrections made for the image shift, rotation, and change of magnification of the defocused image pairs used in the analysis.

Figure 5 shows a row of magnetic permalloy elements ranging from 100–750 nm. Figure 5(a) is an in-focus Lorentz image, which mainly gives mass-thickness, or electrostatic contrast. The retrieved phase image and the phase contour map of the same area using the MTIE method are shown in Figs. 5(b) and (c), respectively. Figure 5(d) is the induction map where color represents the amplitude and direction of the induction. It clearly indicates that the three small elements (B, C and D) have a closure domain structure with vortex geometry, i.e. a stable vortex state with 90° domain walls, while the large element A has a triple-domain configuration with nearly anti-parallel magnetization. *In situ* experiments and calculations show that both the vortex state and triple-domain configuration are in low-energy states; the adoption of the final state depends on the element's aspect ratio (its thickness versus in-plane dimension). Figure 5(e) is a phase profile of the line scan across element B, as marked in Fig. 5(b), similar to the schematics of the total phase shown in Fig. 2(g). The reconstructed vector induction map of element B superimposed on the color code is shown in Fig. 5(g). For comparison, we include in Figs. 5(g)–(j) the phase map of the element B using off-axis electron holography, the maximum area of view for our experimental setup. Figures 5(g) and (h) show the wrapped and unwrapped phase image of the element B, respectively. The reconstructed phase profile and the reconstructed induction distribution of the element are shown in Figs. 5(i) and (j). The results from the MTIE agree well with those from holography, except that the data retrieved from the hologram suffers from noise due to the reference wave passing through the amorphous support film. The MTIE procedure imposes a low-pass filter that suppresses high-frequency noise in the images.

7. Conclusions

We demonstrated that Lorentz-phase microscopy, based on the magnetic transport-of-intensity equation (MTIE), is a promising technique for revealing the local

distribution of magnetization. Although the results agree well with off-axis electron-holography experiments, care must be taken in interpreting the observations, especially in identifying the artifacts induced in the imaging process, i.e. the image alignment of the defocus series including image shift, rotation, and distortion. Since the MTIE method is fast and straightforward, it has a potential in achieving real-time phase retrieval to understand magnetic dynamics at a wide range of length scales.

Acknowledgments

References

1. R. P. Cowburn and M. E. Welland, *Science Italics* **287**, 1466 (2000).
2. J. B. Wedding, M. Li and G.-C. Wang, *J. Magn. Magn. Mater.* **204**, 79 (1999).
3. C. T. Chen, *et al.*, *Phys. Rev. Lett.* **75**, 152 (1995).
4. J. Unguris, D. T. Pierce and R.-J. Celotta, *Rev. Sci. Instrum.* **57**, 1314 (1984).
5. J. N. Chapman, P. R. Aitchison, K. J. Kirk and S. McVitie, *J. Appl. Phys.* **83**, 5321 (1998).
6. P. Grutter, H. J. Mamin and D. Rugar, "Magnetic force microscopy", in: *Scanning Tunneling Microscopy II*, Vol. 28, R. Wiesendanger and H.-J. Gunterodt (eds.) (Springer-Verlag, Berlin, 1992), pp. 151–207.
7. A. Tonomura, N. Osakabe, T. Matsuda, T. Kawasaki, J. Endo, S. Yano and H. Yawada, *Phys. Rev. Lett.* **56**, 792 (1986).
8. M. R. Teague, *J. Opt. Soc. Am.* **73**, 1434 (1983).
9. V. V. Volkov, Y. Zhu and M. De Graef, *Micron* **33**, 411–416 (2002).
10. V. V. Volkov, D. C. Crew, Y. Zhu and L. H. Lewis, *Rev. Sci. Instrum.* **73**, 2298 (2002).
11. D. Gabor, *Proc. Roy. Soc.* **A197**, 454 (1949).
12. D. Paganin and K. A. Nugent, *Phys. Rev. Lett.* **80**, 2586 (1998); T. E. Gureev and K. A. Nugent, *J. Opt. Soc. Am.* **A13**, 1670–1682 (1996); T. E. Gureev, A. Roberts and K. A. Nugent, *ibid.* **A12**, 1942 (1995).
13. Y. Aharonov and D. Bohm, *Phys. Rev.* **115**, 485 (1959).
14. T. T. Wu and C. N. Yang, *Phys. Rev.* **D13**, 3845 (1975).
15. V. V. Volkov and Y. Zhu, accepted for *Phys. Rev. Lett.*
16. H. Hoffmann, *IEEE Trans. Magn.* **MAG-4**, 32 (1968).
17. S. X. Zhou, Y. G. Wang, J. H. Ulvensoen and R. Hoier, *IEEE Trans. Magn.* **30**, 4815 (1994).